Chapter 9

Design of Graphene-Based Metamaterial Absorber and Antenna

Yan Shi and Ying Zhang

Additional information is available at the end of the chapter

http://dx.doi.org/10.5772/intechopen.78608

Abstract

Graphene is a monolayer of carbon atoms arranged in a honeycomb structure which exhibits remarkable properties including high electron mobility, mechanical flexibility, and saturable absorption. In this chapter, the conductivity model of the graphene is first reviewed. Based on the conductivity model of graphene, the equivalent circuit model of graphene is discussed. By varying graphene's chemical potential via external biasing voltage, graphene conductivity can be flexibly tuned in the terahertz and infrared frequencies. With the tunable characteristic, graphene-based metamaterial absorber and reflectarray have been designed. Good performance in these examples illustrates that graphene promises sufficient flexibility in the design of metamaterial devices.

Keywords: graphene, conductivity model, equivalent circuit model, tunable, metamaterial, absorber, reflectarray

1. Introduction

Metamaterial [1–6] has attracted much attention in the scientific communities over the past 20 years. The metamaterial is a macroscopic composite of periodic or non-periodic structures whose scale is smaller than the wavelength. Metamaterials derive their properties not from the properties of base materials but from their newly designed structures. The property of the subwavelength structure in the metamaterial can be described by effective medium parameters [7–12] including electric permittivity and magnetic permeability. The design of the structure allows effective medium parameters to be tailored to special parameters, for example, near-zero values and negative values, and the resultant metamaterials could flexibly manipulate the behavior of electromagnetic waves in ways that have not been conventionally possible

[13–22]. For example, the well-known double negative materials, which was proposed by Veselago [23], can support the backward propagating waves [24], and near-zero material can tunnel electromagnetic waves through very narrow channels [25].

In recent years, metasurfaces have caused huge research interest [26–30]. Metasurfaces may be considered as the two-dimensional counterparts of metamaterials. Due to its subwavelength thickness, metasurfaces are easier to fabricate by using planar fabrication technology. Different from the effective medium characterization of the volume metamaterial, metasurfaces modulate the behaviors of electromagnetic waves through specific boundary conditions. By designing subwavelength-scaled patterns in horizontal dimensions, characteristics of electromagnetic waves including phase, magnitude, and polarization can be flexibly manipulated. One of the most important applications by means of the metasurface is to control the wavefront of the electromagnetic waves by imparting local, gradient phase shift to the incoming waves, which results in generalized Snell's transmission and reflection laws [26].

Graphene [31, 32] consisting of a single layer of carbon atoms arranged in a hexagonal lattice has attracted increasingly attention of the research community due to its extraordinary mechanical, electric, optical, and heating properties. Intrinsic graphene is a zero band-gap semiconductor which is very promising for nanoelectronics applications, because its conduction and valence bands meet at Dirac points. Graphene's transport characteristic and conductivity can be tuned by either electrostatic or magnetostatic gating or via chemical doping [31, 33]. The Fermi level of intrinsic graphene can be engineered to support surface plasmons polariton (SPP) [34, 35]. These fascinating characteristics promise graphene a nature candidate in the metamaterial/metasurface-based devices including absorbers [36–39], cloaks [40], filters [41], antennas [42, 43], nonlinear optical devices [44], etc. In this chapter, we first review the conductivity model and equivalent circuit model of graphene, respectively. Next, a graphene-based metamaterial absorber with good performance including tunable absorbing bandwidth, wide angle, and polarization insensitive characteristic is developed at mid-infrared frequencies. Finally, a wideband tunable graphene-based metamaterial reflectarray is proposed to generate an orbital angular momentum (OAM) vortex wave in terahertz.

2. Conductivity model of graphene

Due to its mono-atomic thickness, graphene can be considered as an infinitesimally thin surface. With graphene's gapless electronic band structure, conductivity is the most appropriate parameter to characterize its electromagnetic properties. Hence the graphene sheet is modeled by surface conductivity, which relates the surface current to the tangential electric field in the graphene plane.

As shown in **Figure 1**, consider a graphene sheet in the presence of an electric field $\vec{E} = \hat{x}E_x$ and a static magnetic field $\vec{B}_0 = \hat{z}B_0$. The electron in graphene is accelerated along −x direction by the electric field force $\vec{F}_e = -\hat{x}eE_x$. As the electron moves with a speed $\vec{v} = -\hat{x}v$, the magnetic

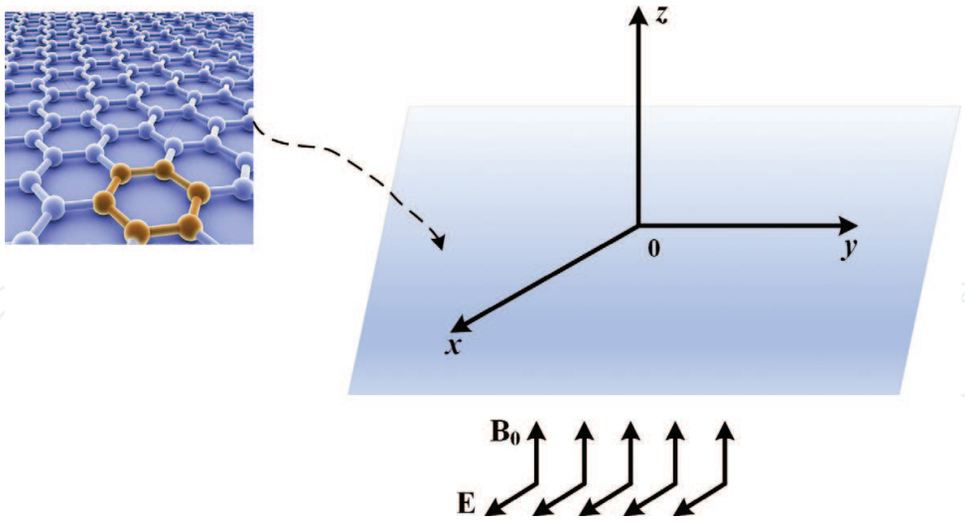

Figure 1. A graphene sheet biased with a static magnetic field.

field force $\vec{F}_m = -e\,\vec{v} \times \vec{B} = -\hat{y}eB_0v$ is generated to deflect the electron toward −y direction. Therefore, the induced current has two components, i.e., $\vec{J} = \hat{x}J_x + \hat{y}J_y = \hat{x}\sigma_{xx}E_x + \hat{y}\sigma_{yx}E_x$. Similarly, in the case of an electric field $\vec{E} = \hat{y}E_y$ and a static magnetic field $\vec{B}_0 = \hat{z}B_0$, the induced current becomes $\vec{J} = \hat{x}J_x + \hat{y}J_y = -\hat{x}\sigma_{yx}E_y + \hat{y}\sigma_{xx}E_y$. Hence, an interesting property of graphene is magnetically induced gyrotropy which can be stated as

$$\vec{J} = \overline{\sigma} \cdot \vec{E}\,, \tag{1}$$

in which

$$\overline{\sigma} = \begin{bmatrix} \sigma_{xx} & -\sigma_{yx} \\ \sigma_{yx} & \sigma_{xx} \end{bmatrix}. \tag{2}$$

The conductivity tensor in Eq. (2) can be determined from Kubo formalism, and the explicit expressions of σ_{xx} and σ_{xy} for zero energy gap are [45, 46]:

$$\sigma_{xx} = \frac{e^2 v_F^2 |eB_0| \hbar(\omega - j2\Gamma)}{-j\pi} \sum_{n=0}^{\infty} \left\{ \frac{n_F(M_n) - n_F(M_{n+1}) + n_F(-M_{n+1}) - n_F(-M_n)}{(M_{n+1} - M_n)\left[(M_{n+1} - M_n)^2 - \hbar^2(\omega - j2\Gamma)^2\right]} + \frac{n_F(-M_n) - n_F(M_{n+1}) + n_F(-M_{n+1}) - n_F(M_n)}{(M_{n+1} + M_n)\left[(M_{n+1} + M_n)^2 - \hbar^2(\omega - j2\Gamma)^2\right]} \right\}, \tag{3}$$

$$\sigma_{yx} = -\frac{e^2 v_F^2 eB_0}{\pi} \sum_{n=0}^{\infty} \left\{ \frac{n_F(M_n) - n_F(M_{n+1}) - n_F(-M_{n+1}) + n_F(-M_n)}{\left[(M_{n+1} - M_n)^2 - \hbar^2(\omega - j2\Gamma)^2\right]} + \frac{n_F(M_n) - n_F(M_{n+1}) - n_F(-M_{n+1}) + n_F(-M_n)}{\left[(M_{n+1} + M_n)^2 - \hbar^2(\omega - j2\Gamma)^2\right]} \right\}, \tag{4}$$

in which $v_F \approx 10^6 m/s$ is the Fermi velocity, $n_F(y) = 1/\{1 + \exp[(y - \mu_c)/(k_B T)]\}$ is Fermi-Dirac distribution, $M_n = \sqrt{2n\hbar v_F^2 |eB_0|}$ is the energy of the nth Landau level, μ_c is chemical potential, $\tau = 1/(2\Gamma)$ is the scattering time, $-e$ is the charge of an electron, $\hbar$ is the reduced Planck's constant, T is temperature, and k_B is Boltzmann constant.

In the low magnetic field limit, Eqs. (3) and (4) can be rewritten as [47]:

$$\sigma_{xx} = \frac{-je^2(\omega - 2j\Gamma)}{\pi\hbar^2}\left[\frac{1}{(\omega - 2j\Gamma)^2}\int_0^\infty \varepsilon\left(\frac{\partial n_F(\varepsilon)}{\partial\varepsilon} - \frac{\partial n_F(-\varepsilon)}{\partial\varepsilon}\right)d\varepsilon - \int_0^\infty \frac{n_F(-\varepsilon) - n_F(\varepsilon)}{(\omega - j2\Gamma)^2 - 4(\varepsilon/\hbar)^2}d\varepsilon\right], \tag{5}$$

$$\sigma_{yx} = -\frac{e^2 v_F^2 eB_0}{\pi\hbar^2}\left[\frac{1}{(\omega + 2j\Gamma)^2}\int_0^\infty \left(\frac{\partial n_F(\varepsilon)}{\partial\varepsilon} + \frac{\partial n_F(-\varepsilon)}{\partial\varepsilon}\right)d\varepsilon + \int_0^\infty \frac{1}{(\omega + j2\Gamma)^2 - 4(\varepsilon/\hbar)^2}d\varepsilon\right], \tag{6}$$

in which ω is radian frequency. Note that Eqs. (5) and (6) are valid under the condition $\sqrt{\hbar|eB_0|v_F^2/c} \le \Gamma$. Specially, in the absence of biased magnetic field, we have $\sigma_{yx} = 0$ and thus graphene is reduced to be isotropic. It is worthwhile pointing out that in Eqs. (5) and (6), there are two terms: the first one is related to intra-band contribution and the second one corresponds to inter-band contribution. The intra-band term in Eq. (5) can be analytically obtained as [48]:

$$\sigma_{xx,\text{intra}} = -j\frac{e^2 k_B T}{\pi\hbar^2(\omega - j2\Gamma)}\left[\frac{\mu_c}{k_B T} + 2\ln\left(e^{-\frac{\mu_c}{k_B T}} + 1\right)\right]. \tag{7}$$

According to Eq. (7), the intra-band term follows the Drude model form. The real part of the intra-band term is greater than zero and its imaginary part is less than zero.

Generally, the inter-band term in Eq. (5) cannot be analytically obtained. However, when $k_B T \le |\mu_c|$ and $k_B T \le \hbar\omega$, the inter-band term in Eq. (5) can be approximately expressed as [46]:

$$\sigma_{xx,\text{inter}} = -j\frac{e^2}{4\pi\hbar}\log\left[\frac{2|\mu_c| - (\omega - j2\Gamma)\hbar}{2|\mu_c| + (\omega - j2\Gamma)\hbar}\right]. \tag{8}$$

It can be seen from Eq. (8) that for $\Gamma = 0$ and $2|\mu_c| > \hbar\omega$, $\sigma_{xx,\text{inter}} = j\sigma''_{xx,\text{inter}}$ becomes a purely imaginary number with a positive imaginary part. In the case of $\Gamma = 0$ and $2|\mu_c| < \hbar\omega$, $\sigma_{xx,\text{inter}} = \sigma'_{xx,\text{inter}} + j\sigma''_{xx,\text{inter}}$ is a complex number, whose imaginary part is still positive and real part is $\sigma'_{xx,\text{inter}} = \sigma_{\min} = \pi e^2/2h$ for $\mu_c \neq 0$. The intra-band conductivity mainly accounts for low-frequency electrical transport and the inter-band conductivity is for the optical excitations.

http://dx.doi.org/10.5772/intechopen.78608

Figure 2 shows real and imaginary parts of the intra-band and intra-band terms of an isotropic graphene surface at 100 GHz and 400 THz for $\Gamma = 0.3291$ meV and $T = 300$ K, respectively. According to **Figure 2**, we can see that at low-terahertz frequencies the conductivity of graphene is mainly governed by the intra-band contribution, while at infrared frequencies, both the intra-band and inter-band conductivities are dominant. In addition, we can know that the intra-band conductivity has a negative imaginary part. **Figure 3** gives the corresponding total conductivities at 100 GHz and 400 THz. It can be observed that the imaginary part of the total conductivity can be positive or negative depending on the operation conditions of the graphene.

One of the main advantages of graphene is that its chemical potential can be tuned by the implementation of a gate voltage or chemical doping. For an isolate graphene sheet, the carrier density n_s is related with μ_c via the following expression [48]

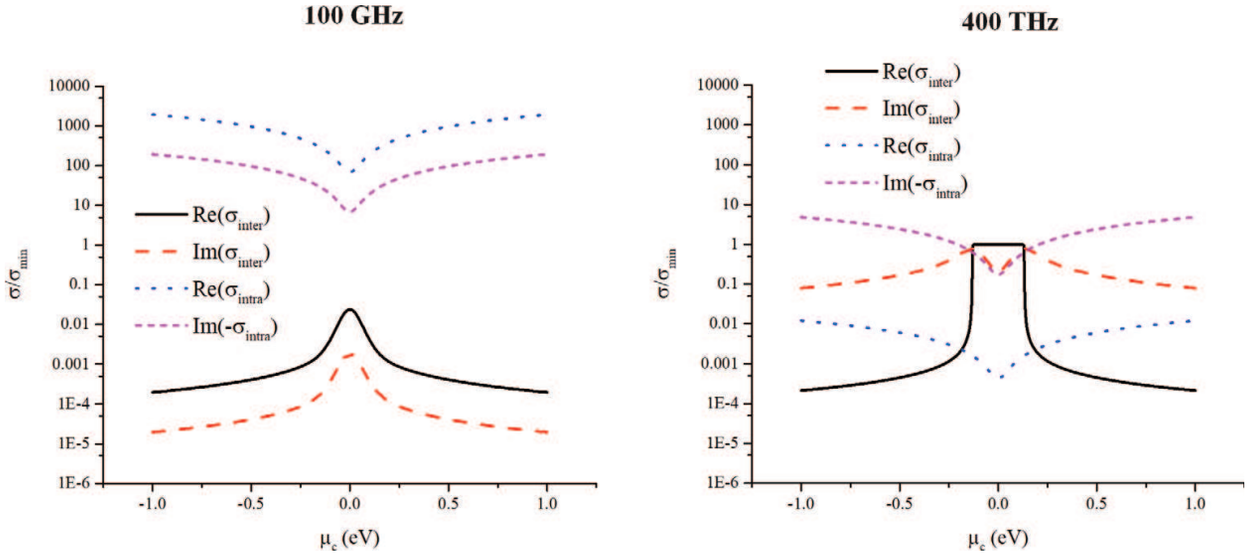

Figure 2. Intraband and interband conductivities of an isotropic graphene sheet at different frequencies.

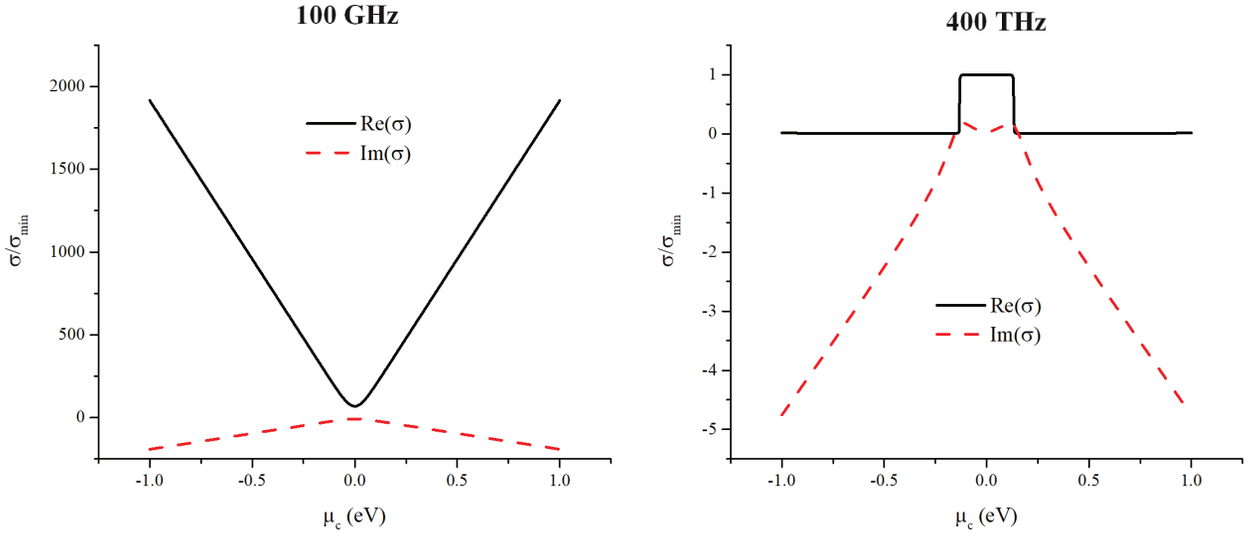

Figure 3. Total conductivities of an isotropic graphene sheet at different frequencies.

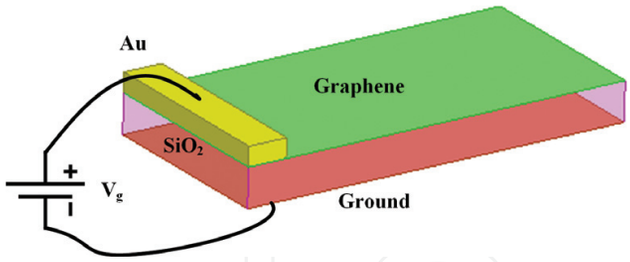

Figure 4. The graphene sheet with an external gate voltage.

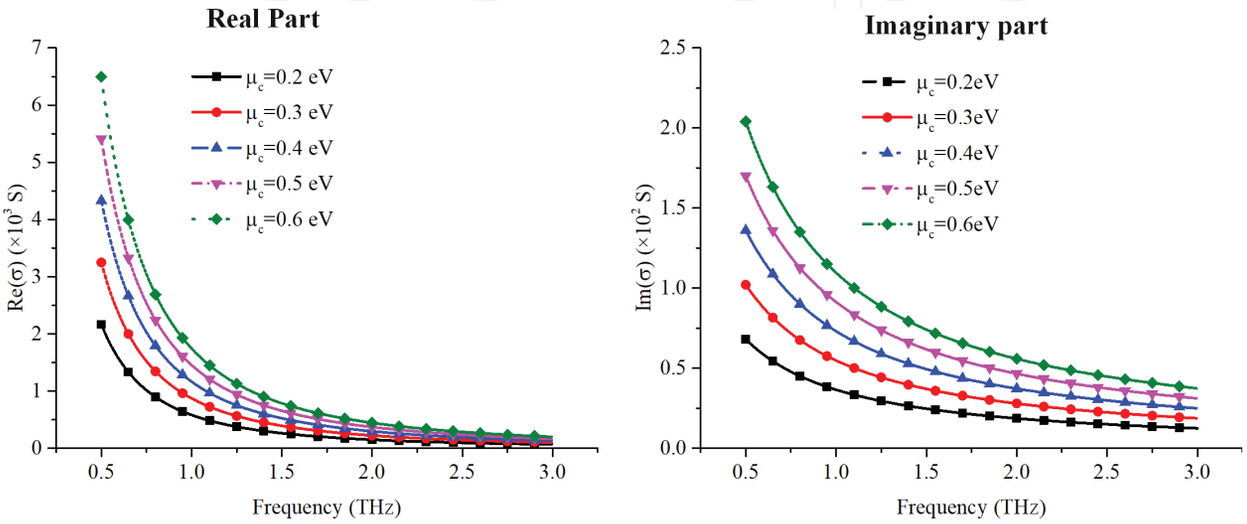

Figure 5. Total conductivity of the graphene as a function of the chemical potential.

$$n_s = \frac{2}{\pi\hbar^2 v_f^2}\int_0^\infty \varepsilon\left[f(\varepsilon) - f\left(\varepsilon + 2\mu_c\right)\right]d\varepsilon. \tag{9}$$

A single-layer graphene is grown on a substrate, for example, oxidized Si, and a gate voltage V_g can be applied, as shown in **Figure 4**. The gate voltage modifies the graphene carrier density as [32]

$$n_s = \varepsilon_0 \varepsilon V_g / te, \tag{10}$$

in which ε_0 and ε are permittivities of free space and the substrate, respectively, and t is the thickness of the substrate. Solving Eqs. (9) and (10), a relation between μ_c and V_g can be obtained. An approximate close-form expression to relate μ_c to V_g can be given as [33]

$$\mu_c = \hbar v_f \sqrt{\frac{\varepsilon_0 \varepsilon}{et} V_g}. \tag{11}$$

Figure 5 shows the conductivity variation of isotropic graphene with chemical potential. Here $\Gamma = 0.3291$ meV and $T = 300$ K. By changing the chemical potential, the conductivity of graphene can be flexibly adjusted, which provides us large degrees of freedom to design tunable graphene-based devices.

3. Equivalent circuit model of multilayer graphene

The isolate graphene sheet can be characterized by its complex conductivity. In some designs of graphene-based metamaterial/metasurface devices, we need to consider electromagnetic wave interaction with the stacked periodic graphene sheets. **Figure 6** shows a stack of graphene sheets separated by material slabs. In order to study plane wave reflection and transmission by a graphene-material stack, an equivalent circuit model [43] is developed in this section. Consider a uniform transverse electromagnetic (TEM) wave normally incident on the multilayer structure. Assume no higher-order modes are excited. Therefore, each graphene sheet is equivalent to a shunt admittance Y_{gi} ($i = 1, 2, \ldots, N$), and each material slab is regarded as a transmission line segment with a characteristic admittance Y_{mi} and an electric length $\theta_i = \beta_i d_i$, in which β_i is the phase constant in each material slab and d_i is the thickness of the material slab. The corresponding equivalent circuit model is depicted in **Figure 7**.

According to the transfer matrix approach, the ABCD matrix can be written as:

$$\begin{bmatrix} A & B \\ C & D \end{bmatrix} = \left(\prod_{i=1}^{N} \begin{bmatrix} 1 & 0 \\ Y_{gi} & 1 \end{bmatrix} \cdot \begin{bmatrix} \cos\theta_i & j\dfrac{1}{Y_{mi}}\sin\theta_i \\ jY_{mi}\sin\theta_i & \cos\theta_i \end{bmatrix} \right) \begin{bmatrix} 1 & 0 \\ Y_{mN+1} & 1 \end{bmatrix}. \tag{12}$$

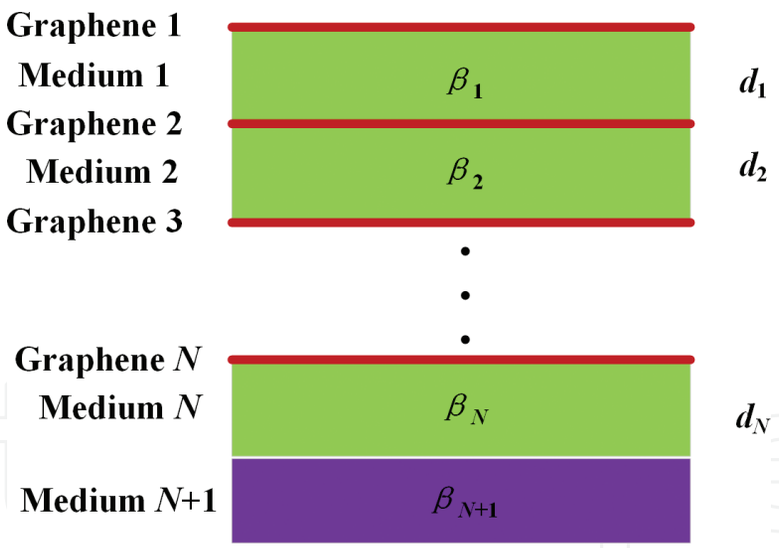

Figure 6. Planar multilayer graphene.

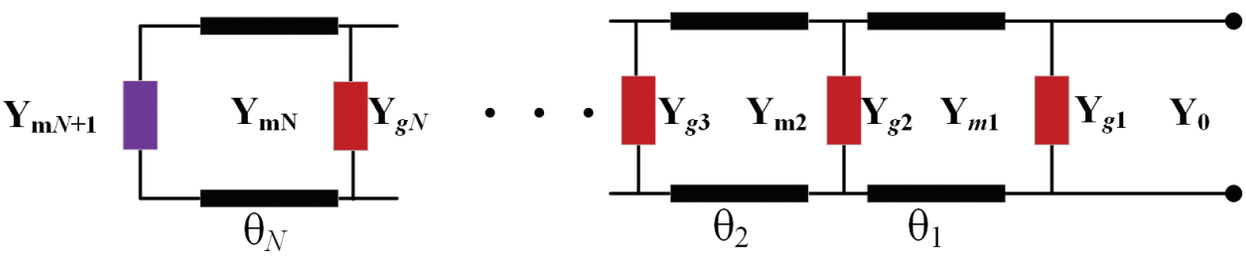

Figure 7. The equivalent circuit model of the multilayer graphene-based structure.

Furthermore, the S parameters can be obtained as:

$$S_{11} = \frac{A + B/Z_0 - CZ_0 - D}{A + B/Z_0 + CZ_0 + D}, S_{12} = \frac{2(AD - BC)}{A + B/Z_0 + CZ_0 + D}, \tag{13}$$

$$S_{21} = \frac{2}{A + B/Z_0 + CZ_0 + D}, S_{22} = \frac{-A + B/Z_0 - CZ_0 + D}{A + B/Z_0 + CZ_0 + D}. \tag{14}$$

To determine the shunt admittance, Y_{gi} of ith graphene sheet given in **Figure 6**, assume ith graphene sheet as an array of graphene patches with a period of D_i, as shown in **Figure 8**. The gap between the graphene patches is g_i ($g_i < D_i$), and permittivities of the material slabs at the top and bottom part of the graphene array are ε_i and ε_{i+1}, respectively. In the case of the normally incident wave, the graphene patch array can be characterized by a surface impedance Z_{gi}, which relates the average tangential components of the total electric field $\vec{E}^{tot}_{\tan}$ and the

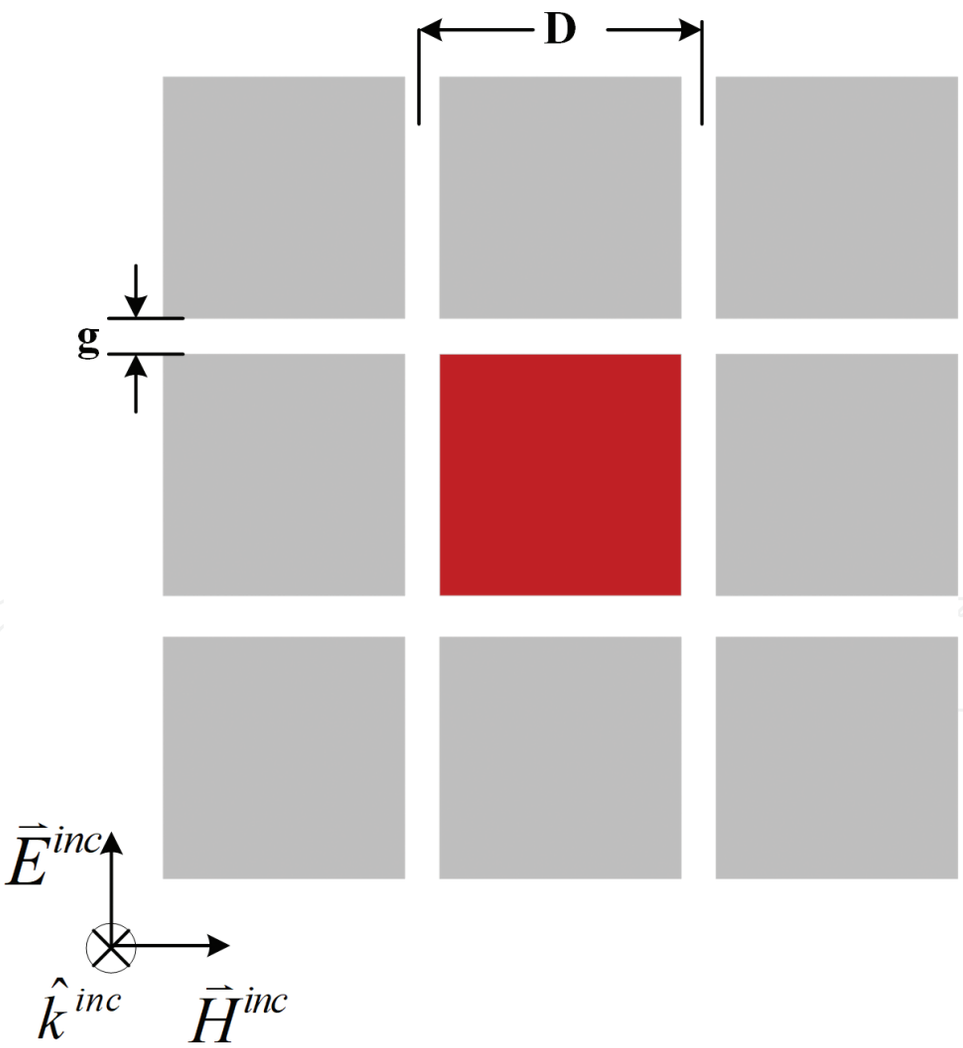

Figure 8. Periodic graphene patch array.

average surface current density $\vec{J}^{ind}$ induced on it. The average boundary condition for the patch array can be written as [49–51]

$$E_{\tan}^{tot} = Z_{gi} \cdot J^{ind}, \tag{15}$$

in which

$$Z_{gi} = \frac{1}{Y_{gi}} = \frac{D_i}{(D_i - g_i)\sigma_i} - j\frac{\pi}{2\omega\varepsilon_{eq}D_i \ln\left[\csc\left(\pi g_i/2D_i\right)\right]}, \tag{16}$$

Here, σ_i is the conductivity of graphene and ε_{eq} is equivalent permittivity with the following expression:

$$\varepsilon_{eqr} = (\varepsilon_i + \varepsilon_{i+1})/2. \tag{17}$$

It is shown that when the gap tends to be zero, the corresponding graphene patch array becomes a whole graphene sheet and thus the surface impedance given by Eq. (16) is reduced to $Z_{gi} = 1/\sigma_i$.

Consider a graphene-based metasurface structure, as shown in **Figure 9**. Here T = 300 K and Γ = 3.2914 meV are used for each graphene sheet. The chemical potential of the top graphene layer is denoted as μ_{c1} and the bottom one is μ_{c2}. Relative permittivity of the silicon material is 11.9. To validate the effectiveness of the equivalent circuit model, we consider three cases. The first case is L1 = 20 μm and μ_{c1} = 0.1 meV and μ_{c2} = 0.2 meV. The corresponding resonant frequency of the metasurface structure obtained by the equivalent circuit is 0.95 THz, which is same as the result obtained by the full-wave simulation. In the second case of L1 = 15 μm and $\mu_{c1} = \mu_{c2}$ = 0.15 meV, the resonant frequencies solved by the equivalent circuit and the full-wave simulation are 1.18 THz and 1.2 THz, respectively. For the third case, i.e., L1 = 12 μm and μ_{c1} = 0.2 meV and μ_{c2} = 0.1 meV, the resonant frequencies solved by two methods are 1.39 THz and 1.4 THz, respectively. **Figure 10** demonstrates the absorption obtained by equivalent circuit and full-wave simulation, in good agreement.

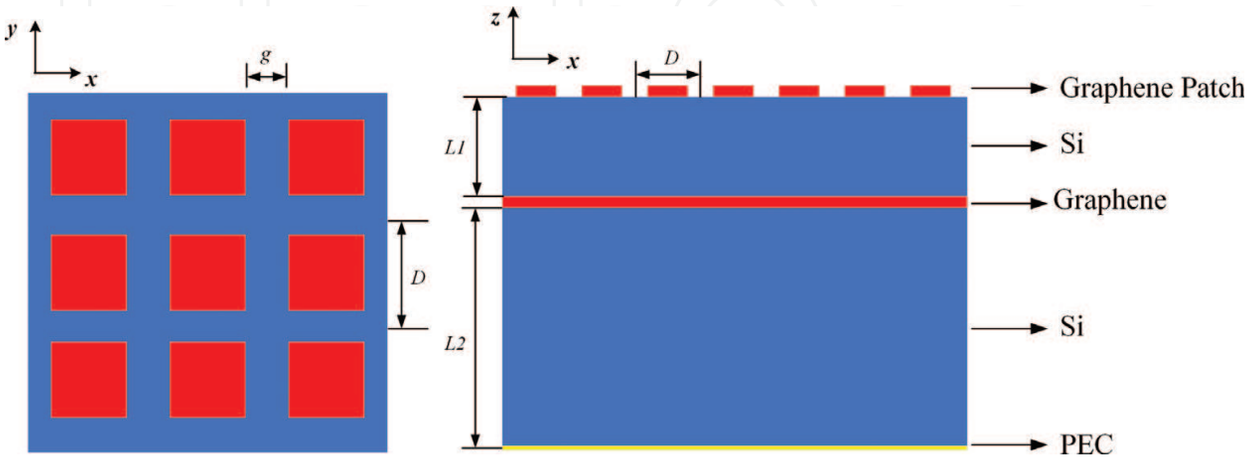

Figure 9. A graphene-based metasurface structure. All dimensions are in micrometer: L1 = 5, D = 20, and g = 2.

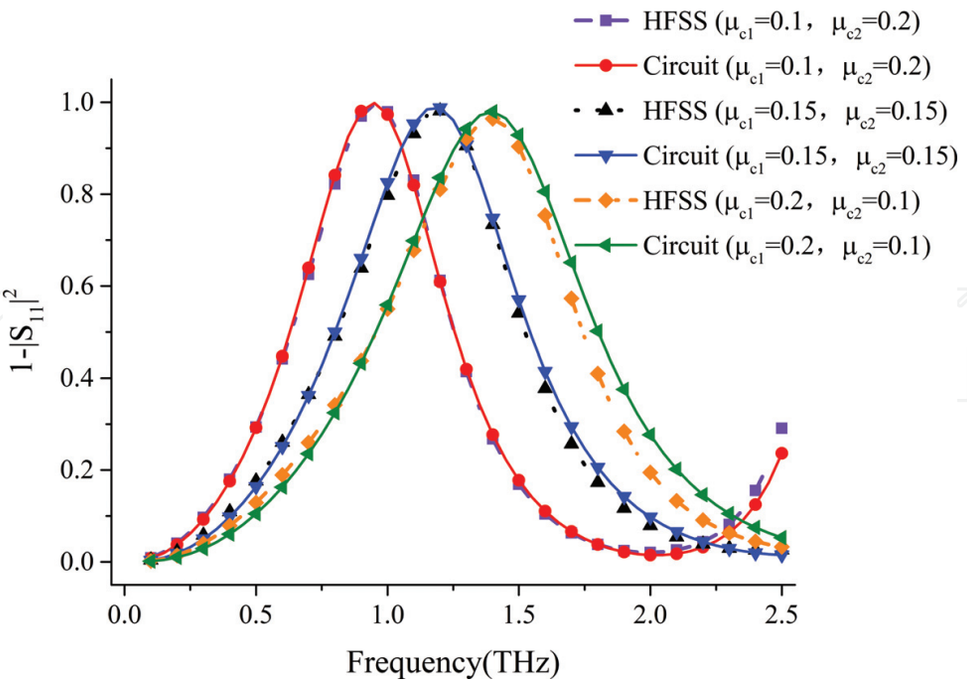

Figure 10. Absorption of the graphene-based metasurface structure.

4. Graphene-based metamaterial absorber

With extraordinary electronic and optical properties, graphene has caused enormous research interest in recent years. The conductivity or carrier density of graphene can be tuned by the chemical potential via an external gate voltage. Various intriguing applications such as tunable cloaks [40], reflectarray [42, 43], nonlinear optical devices [44], etc., have been proposed and experimentally demonstrated. On the other hand, since Landy et al. proposed a thin and near-perfect metamaterial absorber in 2008 [52], various metamaterial absorbers have been demonstrated from microwave to optical frequencies [53, 54]. The fascinating property of the tunable conductivity promises graphene a good candidate for the design of the tunable metamaterial absorber. In this section, a broadband tunable, wide-angle, and polarization-insensitive graphene-based metamaterial absorber is designed.

Figure 11 shows the designed metamaterial absorber. The unit cell of metamaterial absorber with a periodicity of 2 μm consists of four layers from the top to the bottom: a dual ELC unit composed of Au with a thickness of 0.1 μm, a graphene sheet, a BaF2 material with a thickness of 0.24 μm, and an Au material with a thickness of 0.5 μm. **Figure 12** shows the absorbing spectra of the proposed absorber for the chemical potential of μ_c = 0.5 eV when TE- and TM-polarized plane waves are normally incident on the proposed absorber, respectively. It can be observed that for TE polarization, a wide absorption characteristic of 90% with a 41.12% fractional bandwidth from 27.78 to 42.16 THz is obtained. Similarly, the absorbing band for the TM polarization covers from 26.78 to 40.06 THz with a 39.74% fractional bandwidth.

Figures 13 and **14** illustrate the polarization and angular dependences of the proposed absorber with μ_c = 0.5 eV, respectively. As shown in **Figure 13**, when the incident angle varies

http://dx.doi.org/10.5772/intechopen.78608

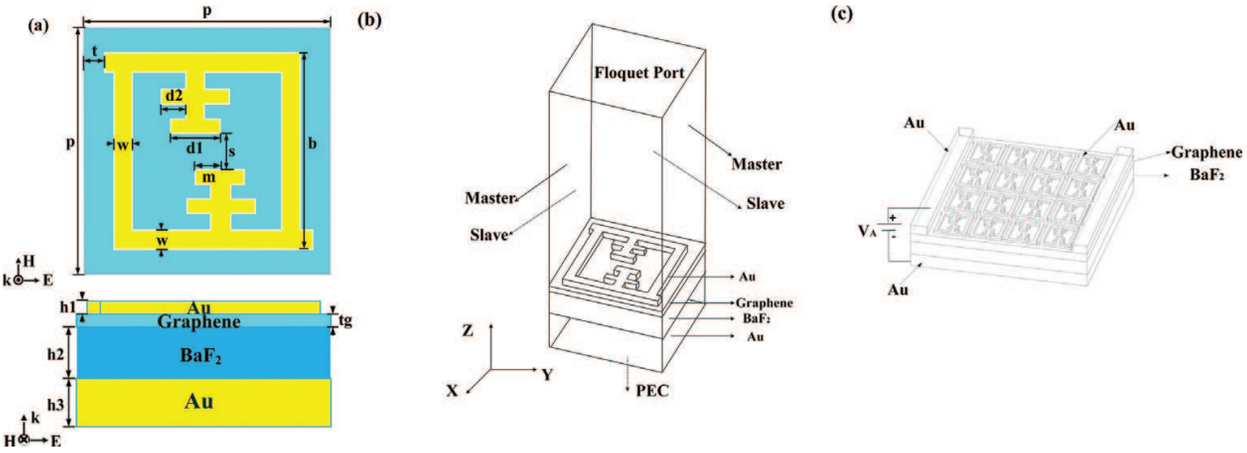

Figure 11. The proposed graphene-based metamaterial absorber. (a) Metamaterial unit cell. (b). Infinite periodic simulation model with periodic boundary conditions (PBC) around the unit cell. (c). A tunable gate voltage applied to the proposed absorber. All dimensions are in micrometer: w = 0.16, s = 0.2, t = 0.12, m = 0.1, d1 = 0.4, and d2 = 0.2. Reprinted from Zhang et al. [38], with permission from the Optical Society of America.

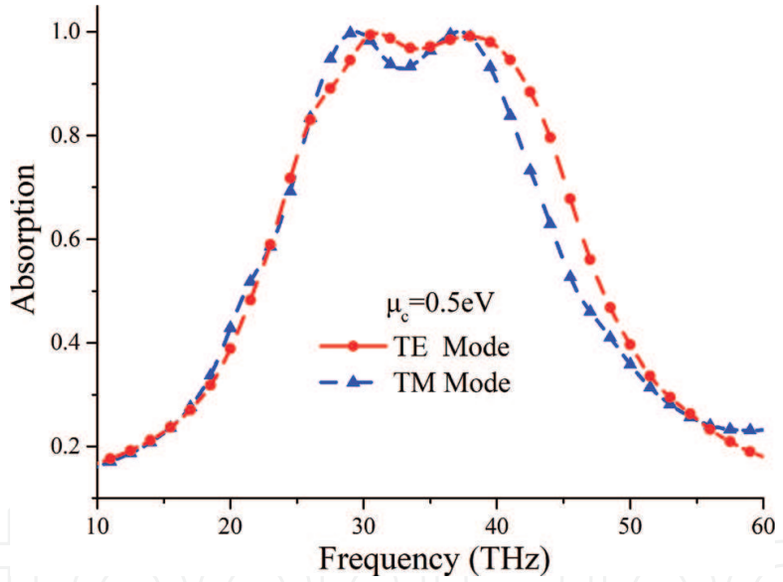

Figure 12. Simulated absorptivity of the proposed absorber with $\mu_c = 0.5$ eV for TE and TM polarizations. Reprinted from Zhang et al. [38], with permission from the Optical Society of America.

from 0 to 60° for both TE and TM polarizations, the absorptions remain above 80% in the whole operating band. Especially, for incident angle below 50°, the absorption over 90% can be achieved. Due to the approximate symmetry of the designed absorber, the absorption is nearly independent of polarization, as shown in **Figure 14**.

Figure 15 demonstrates absorption variation of the proposed absorber with the chemical potential of graphene. For the TE polarization, the fractional absorbing band of the absorption of 90% with $\mu_c = 0.2$ eV is 44.8% from 25.08 to 39.56 THz. With the increase of the chemical potential, the absorption curve has a blue shift accompanied by an approximately unchanged

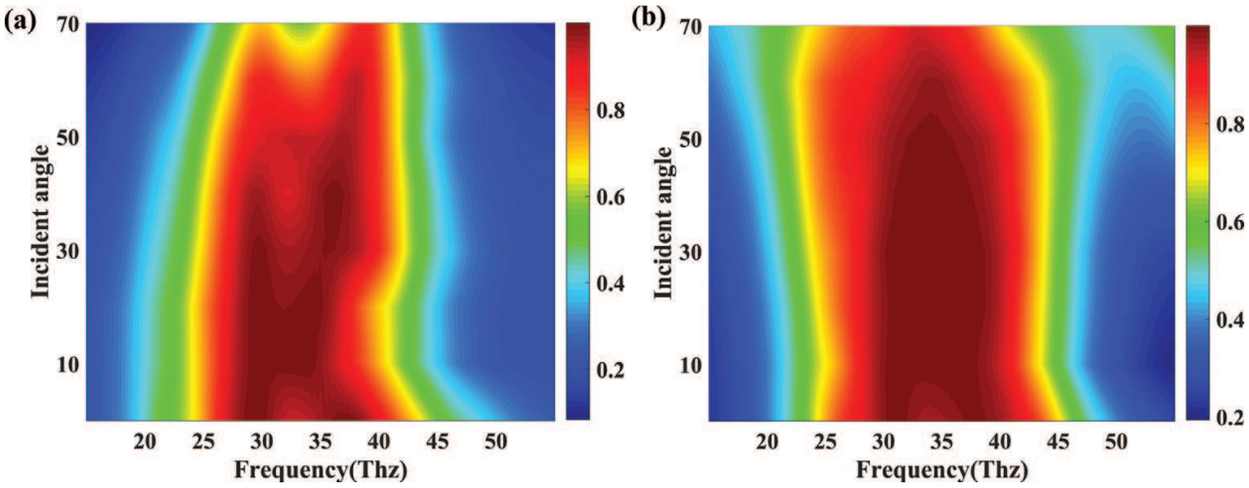

Figure 13. Simulated absorption performance at different incidence angles: (a) TM mode and (b) TE mode. Reprinted from Zhang et al. [38], with permission from the Optical Society of America.

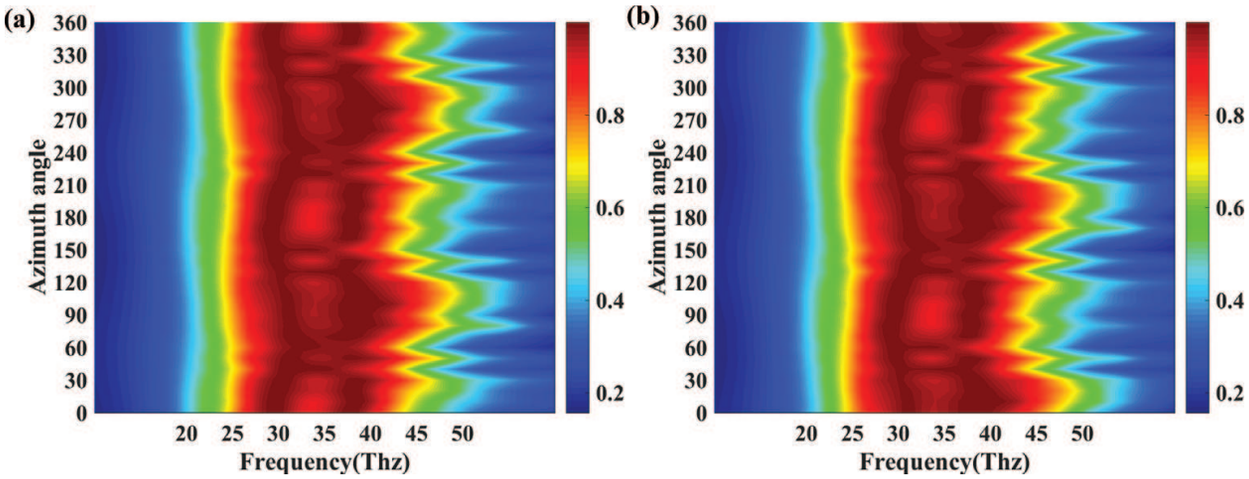

Figure 14. Simulated variation of absorption with frequencies for different azimuth angles: (a) TM mode and (b) TE mode. Reprinted from Zhang et al. [38], with permission from the Optical Society of America.

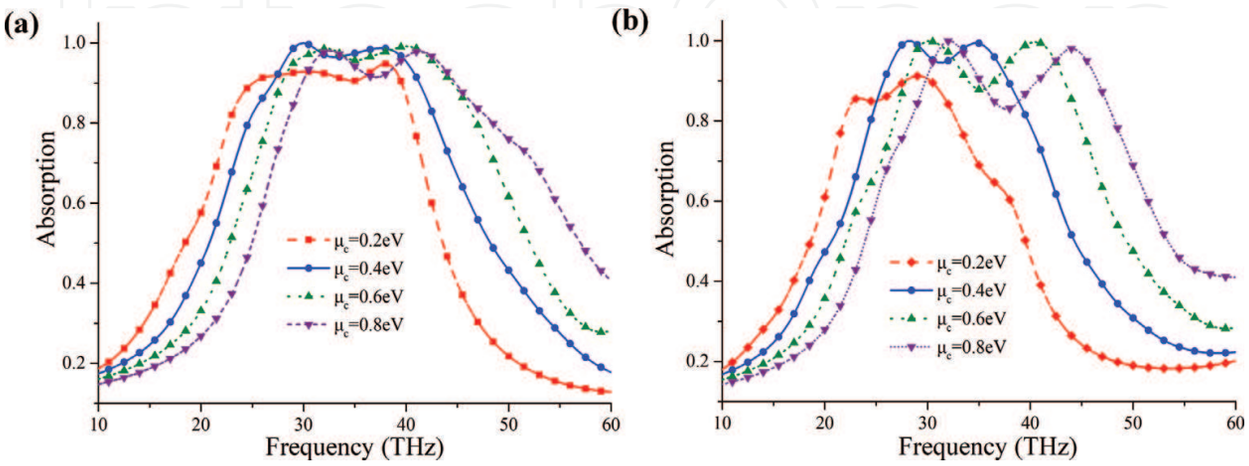

Figure 15. Variation of the absorption with the chemical potential μ_c: (a) TE mode and (b) TM mode. Reprinted from Zhang et al. [38], with permission from the Optical Society of America.

fractional band. By adjusting the chemical potential from 0.2 to 0.8 eV, the absorbing band continuously covers from 25.08 to 44.81 THz. By comparison, for the TM polarization, the fractional absorbing bandwidth firstly increases and then decreases as the chemical potential increases. With the variation of the chemical potential from 0.2 to 0.8 eV, the absorbing band of the absorption of 90% continuously covers from 25.74 to 40.06 THz.

5. Graphene-based metamaterial reflectarray for orbital angular momentum (OAM) vortex wave

The electromagnetic waves carry both linear and angular momentums. Angular momentum comprises spin angular momentum (SAM) and orbital angular momentum (OAM). The SAM is associated with the circular polarization states of electromagnetic beams. The OAM arises from spatial variations of amplitude and phase that render the beam asymmetric around its propagation axis [55, 56]. In 1992, Allen *et al*. found that light beam with an azimuthal phase dependence of exp.($il\phi$) carries an OAM, in which ϕ represents the azimuthal angle and l is the topological charge. For any given l, the OAM vortex wave has l interwinded helical phase fronts and a phase singularity with zero intensity on the beam axis. With a theoretically unlimited range of orthogonal eigenstates, OAM offers new degrees of freedom in communication in addition to traditional linear momentum and polarization degrees of freedom [57–60].

An attractive feature of graphene is that its conductivity is changeable by controlling voltage applied to graphene via an external gate. With this characteristic, a graphene-based metamaterial reflectarray is designed for the generation of the wideband OAM vortex waves with tunable modes in this section. As shown in **Figure 16**, the designed reflectarray with a size of $10\times 10\lambda$ comprises 12 regions, each of which has the same azimuthal angle. Here, λ is wavelength in free space at the frequency of 2.3 THz. In each region, a same graphene-based metamaterial structure is designed. By tuning the conductivities of the graphene sheets in the jth region, the reflection phase of $\pi lj/6$ ($j = 1, \ldots,12$) is achieved such that the whole reflectarray can generate a helical profile of exp.($il\phi$). To guarantee independently adjustable conductivities

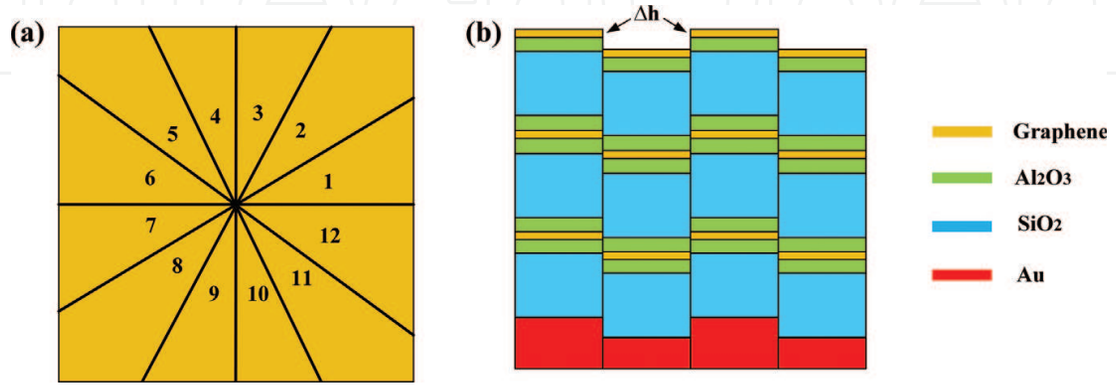

Figure 16. Schematic diagram of the designed reflectarray. (a) The whole array divided into 12 regions, each of which is filled by the same metamaterial unit cells. (b) The side view of the reflectarray. Reprinted from Shi et al. [43], with permission from the IEEE.

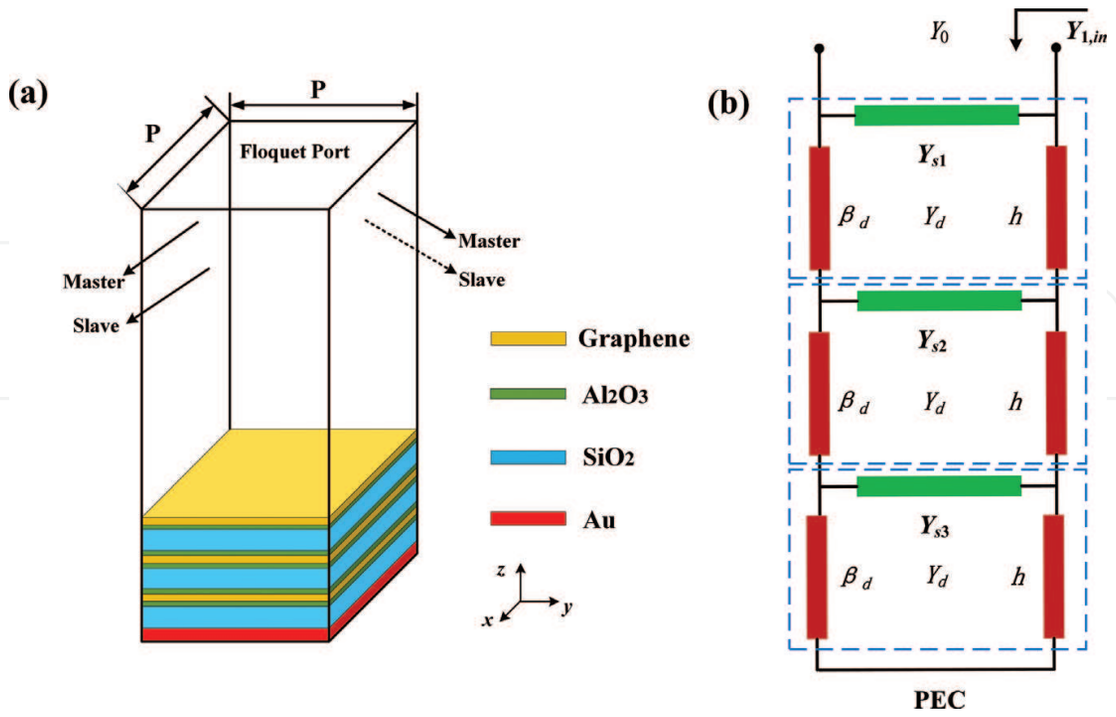

Figure 17. The graphene-based metamaterial unit cell and its equivalent circuit model: (a) the unit cells and (b) the equivalent circuit model. Reprinted from Shi et al. [43], with permission from the IEEE.

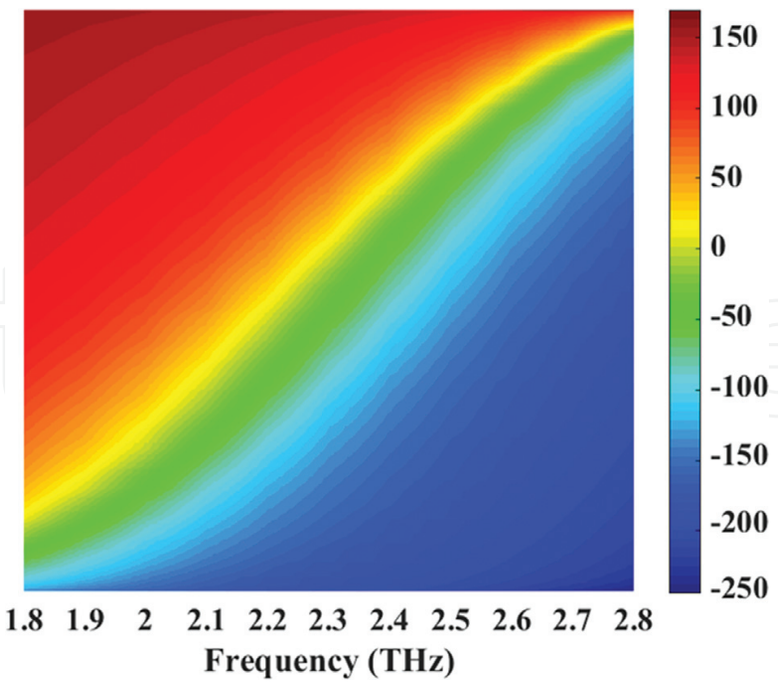

Figure 18. Reflection phase range for all possible chemical potentials of three graphene layers in a wide frequency band from 1.8 THz to 2.8 THz. Reprinted from Shi et al. [43], with permission from the IEEE.

http://dx.doi.org/10.5772/intechopen.78608

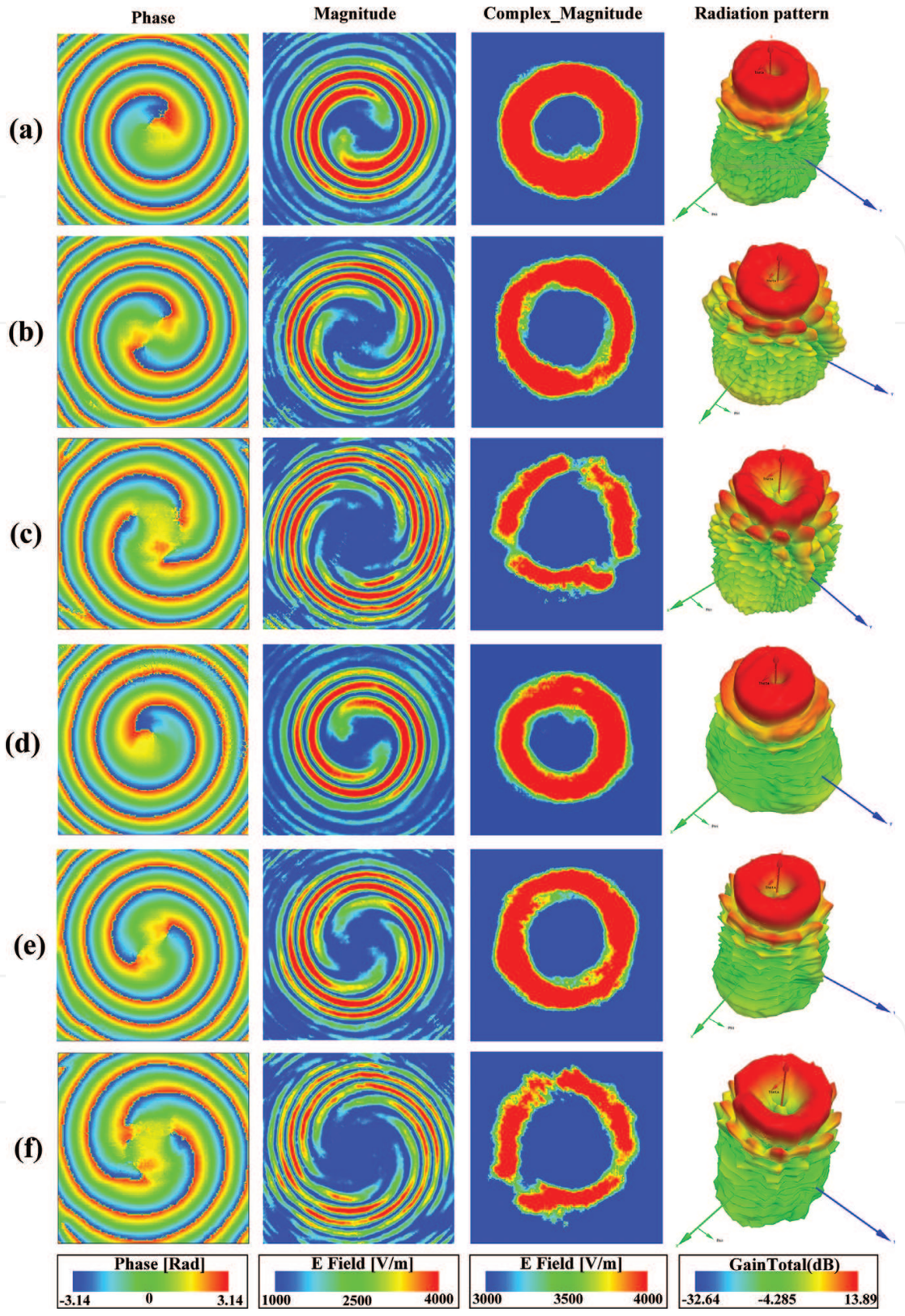

Figure 19. The OAM beams with the different modes: (a) $l = 1$, (b) $l = 2$, (c) $l = 3$, (d) $l = -1$, (e) $l = -2$, and (f) $l = -3$. Reprinted from Shi et al. [43], with permission from the IEEE.

of the graphene sheets in each region, a small height difference Δh is introduced to ensure the insulation between two adjacent regions, as shown in **Figure 16(b)**.

To obtain a desirable reflection phase in each region, a metamaterial unit cell composed of a three-layer sandwich structure has been designed, as shown in **Figure 17**. Each sandwich structure comprises graphene/Al_2O_3/SiO_2 materials from the top to the bottom. An insulating layer of Al_2O_3 material is inserted between two adjacent sandwich structures. A ground consisting of an Au material is placed at the bottom of the unit cell. The designed unit cell periodicity is P = 20 μm, and the thicknesses of SiO_2, Al_2O_3, and Au materials are 12 μm, 10 nm, and 5 μm, respectively. In each sandwich structure, an external DC voltage is applied between the graphene layer and the SiO_2 layer to control the conductivity of graphene. For convenience, the chemical potentials of the graphene layers from the top to the bottom are denoted as "μ_{c1}," "μ_{c2}," and "μ_{c3}," respectively. With the equivalent circuit model given in **Figure 17(b)**, the maximum reflection phase range of the proposed unit cell can be obtained. As shown in **Figure 18**, the reflection phase range of the proposed unit cell can cover 360° in a wide frequency band from 1.8 to 2.8 THz, when three chemical potentials independently vary from −1 to 1 eV.

A wideband horn antenna as the excitation is used to generate a wave incident on the reflectarray. **Figure 19** shows the OAM vortex waves with different modes generated by the reflectarray at 2.3 THz. We can clearly observe the spiral phase distributions of the OAM

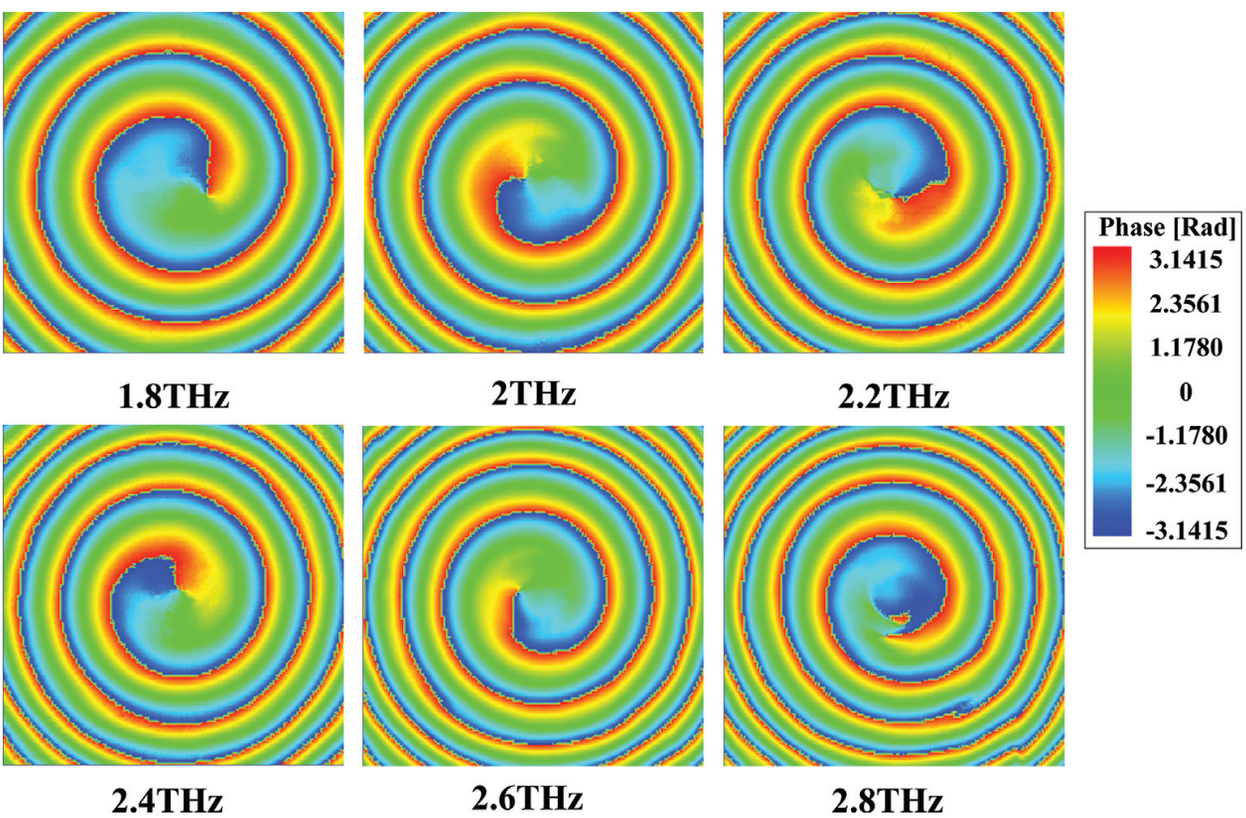

Figure 20. Simulated OAM beams with $l = 1$ mode at different frequencies. Reprinted from Shi et al. [43], with permission from the IEEE.

vortex waves with $l = \pm 1$, $l = \pm 2$, and $l = \pm 3$ modes and the doughnut-shaped intensity distributions. Note that the radiation patterns with singularity in the center greatly reduce the coupling between the reflectarray and the horn antenna. With the reflection phase range of 360° in a wide frequency band from 1.8 to 2.8 THz, as shown in **Figure 18**, the OAM vortex waves can be generated by the proposed reflectarray in the wide frequency band, as shown in **Figure 20**. It is observed that the desirable spiral phase distributions can be obtained in the whole frequency band.

6. Conclusion

In sum, several characteristics of graphene including the conductivity model and equivalent circuit model have been presented. Two graphene-based devices, i.e., metamaterial absorber and metamaterial reflectarray, have been designed. By varying graphene's chemical potential, the wideband tunable absorption for the designed absorber and the broadband tunable OAM modes for the developed reflectarray have been demonstrated, respectively. Graphene provides more degrees of freedom for the design of the tunable metamaterial systems.

Acknowledgements

This work is supported by National Natural Science Foundation of China under Contract 61771359 Fundamental Research Funds for the Central Universities (No. JBF180202), and Technology Innovation Research Project of the CETC.

Conflict of interest

No conflict of interest was reported by the authors.

Author details

Yan Shi* and Ying Zhang

*Address all correspondence to: shiyan@mail.xidian.edu.cn

School of Electronic Engineering, Xidian University, Xi'an, Shaanxi, China

References

[1] Caloz C, Itoh T. Electromagnetic Metamaterials: Transmission Line Theory and Microwave Applications. New Jersey: Wiley; 2005. 376 p. DOI: 10.1002/0471754323

[2] Engheta N, Ziolkowski RW. Metamaterials Physics and Engineering Explorations. New Jersey: New IEEE Press; 2006. 440p. DOI: 10.1002/0471784192

[3] Munk BA. Metamaterials: Critique and Alternatives. New Jersey: Wiley; 2008. 189 p. DOI: 10.1002/9780470423875

[4] Cui TJ, Smith DR, Liu RP. Metamaterials Theory, Design and Applications. New York: Springer; 2010. p. 367. DOI: 10.1007/978-1-4419-0573-4

[5] Werner DH, Kwon DH. Transformation Electromagnetics and Metamaterials Fundamental Principles and Applications. London: Springer; 2014. p. 499. DOI: 10.1007/978-1-4471-4996-5

[6] Werner DH. Broadband Metamaterials in Electromagnetics: Technology and Application. Danvers: Pan Stanford; 2017. p. 371. DOI: 10.4032/9781315364438

[7] Martini E, Sardi GM, Maci S. Homogenization processes and retrieval of equivalent constitutive parameters for multisurface-metamaterials. IEEE Transactions on Antennas and Propagation. 2014;**62**:2081-2092. DOI: 10.1109/TAP.2014.2300169

[8] Simovski CR. Material parameters of metamaterials (a review). Optics and Spectroscopy. 2009;**107**:726-753. DOI: 10.1134/S0030400X09110101

[9] Smith DR, Vier DC, Koschny Th, Soukoulis CM. Electromagnetic parameter retrieval from inhomogeneous metamaterials, Physical Review E. 2005;**71**:036617. DOI: 10.1103/PhysRevE.71.036617

[10] Shi Y, Li ZY, Li K, Li L, Liang CH. A retrieval method of effective electromagnetic parameters for inhomogeneous metamaterials. IEEE Transactions on Microwave Theory and Technology. 2017;**65**:1160-1178. DOI: 10.1109/TMTT.2016.2638424

[11] Shi Y, Hao T, Li L, Liang CH. An improved NRW method to extract electromagnetic parameters of metamaterials. Microwave and Optical Technology Letters. 2016;**58**:647-652. DOI: 10.1002/mop

[12] Shi Y, Li ZY, Li L, Liang CH. An electromagnetic parameters extraction method for metamaterials based on phase unwrapping technique. Wave Random Complex. 2016;**26**:417-433. DOI: 10.1080/17455030.2016.1165899

[13] Pendry JB, Schurig D, Smith DR. Controlling electromagnetic fields. Science. 2006;**312**:1780-1782. DOI: 10.1126/science.1125907

[14] Leonhardt U. Optical conformal mapping. Science. 2006;**312**:1777-1780. DOI: 10.1126/science.1126493

[15] Lai Y, Chen H, Zhang Z, Chan CT. Complementary media invisibility cloak that cloaks objects at a distance outside the cloaking shell. Physical Review Letters. 2009;**102**:033901. DOI: 10.1103/PhysRevLett.102.093901

[16] Li L, Huo FF, Zhang YM, Chen Y, Liang CH. Design of invisibility anti-cloak for two-dimensional arbitrary geometries. Optics Express. 2013;**21**:9422-9427. DOI: 10.1364/OE.21.009422

[17] Huo FF, Li L, Li T, Zhang YM, Liang CH. External invisibility cloak for multiobjects with arbitrary geometries. IEEE Antennas and Wireless Propagation Letters. 2014;**13**:273-276. DOI: 10.1109/LAWP.2014.2304640

[18] Shi Y, Tang W, Liang CH. A minimized invisibility complementary cloak with a composite shape. IEEE Antennas and Wireless Propagation Letters. 2014;**13**:1800-1803. DOI: 10.1109/LAWP.2014.2363875

[19] Shi Y, Zhang L, Tang W, Li L, Liang CH. Design of a minimized complementary illusion cloak with arbitrary position. International Journal of Antennas and Propagation. 2015: 932495. DOI: 10.1155/2015/932495

[20] Shi Y, Tang W, Li L, Liang CH. Three-dimensional complementary invisibility cloak with arbitrary shapes. IEEE Antennas and Wireless Propagation Letters. 2015;**14**:1550-1553. DOI: 10.1109/LAWP.2015.2412171

[21] Zhang L, Shi Y, Liang CH. Optimal illusion and invisibility of multilayered anisotropic cylinders and spheres. Optics Express. 2016;**24**:23333-23352. DOI: 10.1364/OE.24.023333

[22] Shi Y, Zhang L. Cloaking design for arbitrarily shape objects based on characteristic mode method. Optics Express. 2017;**25**:32263-32279. DOI: 10.1364/OE.25.032263

[23] Veselago V. The electrodynamics of substances with simultaneously negative values of ε and μ. Soviet Physics Uspekhi. 1968;**10**:509-514. DOI: 10.1070/PU1968v010n04ABEH003699

[24] Grbic A, Eleftheriades GV. Experimental verification of backward-wave radiation from a negative refractive index metamaterial. Journal of Applied Physics. 2002;**92**:5930-5935. DOI: 10.1063/1.1513194

[25] Edwards B, Alu A, Young ME, Silveirinha M, Engheta N. Experimental verification of epsilon-near-zero metamaterial coupling and energy squeezing using a microwave waveguide. Physical Review Letters. 2008;**100**:033903. DOI: 10.1103/PhysRevLett.100.033903

[26] Yu N, Genevet P, Kats MA, Aieta F, Tetienne JP, Capasso F, Gaburro Z. Light propagation with phase discontinuities: Generalized laws of reflection and refraction. Science. 2011; **334**:333-337. DOI: 10.1126/science.1210713

[27] Ni XJ, Emani NK, Kildishev AV, Boltasseva A, Shalaev VM. Broadband light bending with plasmonic nanoantenna. Science. 2012;**335**:427. DOI: 10.1126/science.1214686

[28] Sun S, He Q, Xiao S, Xu Q, Li X, Zhou L. Grandient-index meta-surfaces as a bridge linking propagating waves and surfaces waves. Nature Materials. 2012;**11**:426-431. DOI: 10.1038/nmat3292

[29] Chen HT, Taylor AJ, Yu N. A review of metasurface: Physics and applications. Reports on Progress in Physics. 2016;**79**:076401. DOI: 10.1088/0034-4885/79/7/076401

[30] Ding F, Pors A, Bozhevolnyi SI. Gradient metasurface: A review of fundamentals and applications. Reports on Progress in Physics. 2018;**81**:026401. DOI: 10.1088/1361-6633/aa8732

[31] Novoselov KS, Geim AK, Morozov SV, Jiang D, Zhang Y, Dubonos SV, Grigorieva IV, Firsov AA. Electric field effect in atomically thin carbon films. Science. 2004;**306**:5696. DOI: 10.1126/science.1102896

[32] Novoselov KS, Geim AK, Morozov SV, Jiang D, Katsnelson MI, Grigorieva IV, Dubonos SV, Firsov AA. Two-dimensional gas of massless dirac fermions in graphene. Nature. 2005;**438**: 197-200. DOI: 10.1038/nature04233

[33] Gomez-Diaz JS, Perruisseau-Carrier J. Graphene-based plasmonic switches at near infrared frequencies. Optics Express. 2013;**21**:15490-15504. DOI: 10.1364/OE.21.015490

[34] Vakil A, Engheta N. Transformation optics using graphene. Science. 2011;**332**:1291-1294. DOI: 10.1126/science.1202691

[35] Grigorenko AN, Polini M, Novoselov KS. Graphene plasmonics. Nature Photonics. 2012; **6**:749-758. DOI: 10.1038/nphoton.2012.262

[36] Su Z, Yin J, Zhao X. Terahertz dual-band metamaterial absorber based on graphene/MgF2 multilayer structures. Optics Express. 2015;**23**:1679-1690. DOI: 10.1364/OE.23.001679

[37] Ning R, Bao J, Jiao ZXY. Omnidirectional polarization-insensitive tunable absorption in graphene metamaterial of nanodisk structure. Journal of Applied Physics. 2015;**118**: 203101. DOI: 10.1063/1.4936222

[38] Zhang Y, Shi Y, Liang CH. Broadband tunable graphene-based metamaterial absorber. Optical Materials Express. 2016;**9**:3036-3044. DOI: 10.1364/OME.6.003036

[39] Wang Y, Song M, Pu M, Gu Y, Hu G, Zhao Z, Wang C, Yu H, Luo X. Stacked graphene for tunable terahertz absorber with customized bandwidth. Plasmonics. 2016:1-6. DOI: 10.1007/s11468-015-0162-5

[40] Farhat M, Rockstuhl C, Bağc H. A 3D tunable and multi-frequency graphene plasmonic cloak. Optics Express. 2013;**21**:12592-12603. DOI: 10.1364/OE.21.012592

[41] Wei Z, Li X, Yin J, Huang R, Liu Y, Wang W, Liu H, Meng H, Liang R. Active plasmonic band-stop filters based on graphene metamaterial at THz wavelengths. Optics Express. 2016;**24**:14344-14351. DOI: 10.1364/OE.24.014344

[42] Carrasco E, Perruisseau-Carrier J. Reflectarray antenna at terahertz using graphene. IEEE Antennas and Wireless Propagation Letters. 2013;**12**:253-256. DOI: 10.1109/LAWP.2013. 2247557

[43] Shi Y, Zhang Y. Generation of wideband tunable orbital angular momentum vortex waves using graphene metamaterial reflectarray. IEEE Access. 2018;**6**:5341-5347. DOI: 0.1109/ ACCESS.2017.2740323

[44] Nikolaenko AE, Papasimakis N, Atmatzakis E, Luo Z, Shen ZX, De Angelis F, Boden SA, Di Fabrizio E, Zheludev NI. Nonlinear graphene metamaterial. Applied Physics Letters. 2012;**100**:181109. DOI: 10.1063/1.4711044

[45] Gusynin VP, Sharapov SG, Carbotte JP. Magneto-optical conductivity in graphene. Journal of Physics: Condensed Matter. 2007;**19**:125429. DOI: 10.1088/0953-8984/19/2/026222

[46] Gusynin VP, Sharapov SG, Carbotte JP. Sum rules for the optical and hall conductivity in graphene. Physical Review B. 2007;**75**:5407. DOI: 10.1103/PhysRevB.75.165407

[47] Gusynin VP, Sharapov SG, Carbotte JP. On the universal ac optical background in graphene. New Journal of Physics. 2009;**11**:095013. DOI: 10.1088/1367-2630/11/9/095013

[48] Hanson GW. Dyadic greens functions and guided surface waves for a surface conductivity model of graphene. Journal of Applied Physics. 2008;**103**:064302. DOI: 10.1063/1.2891452

[49] Luukkonen O, Simovski C, Granet G, Goussetis G, Lioubtchenko D, Räisänen AV, Tretyakov SA. Simple and accurate analytical model of planar grids and high-impedance surfaces comprising metal strips or patches. IEEE Transactions on Antennas and Propagation. 2008;**56**:1624-1632. DOI: 10.1109/TAP.2008.923327

[50] Padooru YR, Yakovlev AB, Kaipa CSP, Hanson GW, Medina F, Mesa F. Dual capacitive-inductive nature of periodic graphene patches: Transmission characteristics at low-terahertz frequencies. Physical Review B. 2013;**87**:115401. DOI: 10.1103/PhysRevB.87.115401

[51] Huang X, Zhang X, Hu Z, Aqrrli M, Alburaikan A. Design of broadband and tunable terahertz absorbers based on graphene metasurface: Equivalent circuit model approach. IET Microwaves, Antennas & Propagation. 2015;**9**:307-312. DOI: 10.1049/iet-map.2014.0152

[52] Landy NI, Sajuyigbe S, Mock JJ, Smith DR, Padilla WJ. Perfect metamaterial absorber. Physical Review Letters. 2008;**100**:207402. DOI: 10.1103/PhysRevLett.100.207402

[53] Li L, Yang Y, Liang CH. A wide-angle polarization-insensitive ultra-thin metamaterial absorber with three resonant modes. Journal of Applied Physics. 2011;**110**:063702. DOI: 10.1063/1.3638118

[54] Shi Y, Li YC, Hao T, Li L, Liang CH. A design of ultra-broadband metamaterial absorber. Wave Random Complex. 2017;**27**:381-391. DOI: 10.1080/17455030.2016.1250974

[55] Allen L, Beijersbergen MW, Spreeuw RJC, Woerdman JP. Orbital angular-momentum of light and the transformation of Laguerre–Gaussian laser modes. Physical Review A. 1992;**45**:8185-8189. DOI: 10.1103/PhysRevA.45.8185

[56] Allen L, Padgett MJ, Babiker M. The orbital angular momentum of light. Progress in Optics. 1999;**39**:291-372. DOI: 10.1016/S0079-6638(08)70391-3

[57] Thidé B, Then H, Sjöholm J, Palmer K, Bergman J, Carozzi TD, Istomin YN, Ibragimon NH, Khamitova R. Utilization of photon orbital angular momentum in the low-frequency

radio domain. Physical Review Letters. 2007;**99**:087701. DOI: 10.1103/PhysRevLett.99.087701

[58] Uchida M, Tonomura A. Generation of electron beams carrying orbital angular momentum. Nature. 2010;**464**:737-739. DOI: 10.1038/nature08904

[59] Yu S, Li L, Shi G, Zhu C, Zhou X, Shi Y. Design, fabrication, and measurement of reflective metasurface for orbital angular momentum vortex wave in radio frequency domain. Applied Physics Letters. 2016;**108**:121904. DOI: 10.1063/1.4944789

[60] Yu S, Li L, Shi G, Zhu C, Shi Y. Generating multiple orbital angular momentum vortex beams using a metasurface in radio frequency domain. Applied Physics Letters. 2016;**108**: 241901. DOI: 10.1063/1.4953786